# RCMDD: A Denoising Architecture for Improved Recovery of Reflectance Confocal Microscopy Images of Skin from Compressive Samples

Fernando X. Arias\*†, Heidy Sierra\*‡ and Emmanuel Arzuaga\*†‡
\*Laboratory for Applied Remote Sensing, Imaging and Photonics
†Department of Electrical and Computer Engineering
‡Department of Computer Science and Engineering
University of Puerto Rico Mayaguez
Email: {fernando.arias, heidy.sierra1, emmanuel.arzuaga}@upr.edu

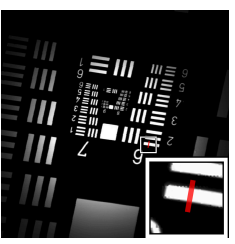
Abstract—The Compressive Sensing (CS) framework has demonstrated improved acquisition efficiency on a variety of clinical applications. Of interest to this work is Reflectance Confocal Microscopy (RCM), where CS can influence a drastic reduction in instrumentation complexity and image acquisition times. However, CS introduces the disadvantage of requiring a time consuming and computationally intensive process for image recovery. To mitigate this, the current document details our preliminary work on expanding a Deep-Learning architecture for the acquisition and fast recovery of RCM images using CS. We show preliminary recoveries of RCM images of both a synthetic target and heterogeneous skin tissue using a stateof-the-art network architecture from compressive measurements at various undersampling rates. In addition, we propose an application-specific addition to an established network architecture, and evaluate its ability to further increase the accuracy of recovered CS RCM images and remove visual artifacts. Our initial results show that it is possible to recover compressively sampled images at near-real time rates with comparable quality to established computationally intensive and time-consuming optimization-based methods common in CS applications.

Index Terms—compressive sensing, deep learning, reflectance confocal microscopy, skin imaging

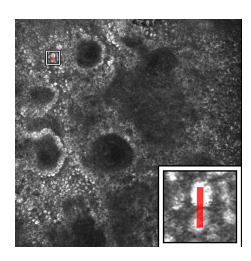
# I. INTRODUCTION

Reflectance Confocal Microscopy (RCM) is an optical imaging technique that possesses the ability to perform non-invasive, in vivo and/or ex-vivo analysis of cell morphology across several optically-sectioned layers of highly heterogeneous tissue [1] [2]. It has found important uses in clinical environments, where it allows time-efficient and non-destructive inspection of basal cells in the dermoepidermal junction region, which facilitates early detection of the presence of cutaneous melanoma [3]. The non-invasiveness of this imaging technique provides advantages for both physicians and patients over traditional invasive procedures, such as Mohs surgery [4]. RCM technology has matured to the point of providing imaging resolution comparable to that of traditional histology,

F.A. is supported by a scholarship grant from the Instituto para la Formacion y Aprovechamiento de Recursos Humanos (IFARHU) office of the government of the Republic of Panama. This material is based upon work supported by the National Science Foundation under Grant No. OAC-1750970.







(b) Skin Slice RCM Image

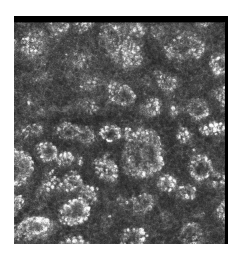
Fig. 1: Left: RCM image of U.S. Air Force Test Chart (USAF-1951) target. Right: Slice 40 of a skin stack captured with an RCM, showing a layer of basal cells. Outlined in red are the regions of Interest for qualitative results in both considered RCM images.

which involves the analysis of  $5\,\mu m$  thin sections of tissue [5]. However, the process of capturing the large areas required for effective clinical evaluation is time-consuming and requires the allocation of time-sensitive computational resources.

Previous work on the applied use of the properties of the Compressive Sensing (CS) framework to increase acquisition efficiency of RCM images for devices in the field has been previously studied [6]. Regarding instrumentation design, several approaches incorporate differing methods of acquiring optically-sectioned random projections through arrays of spatially-distributed pinholes to acquire the linear combinations of the data points of an image required for recovery of CS samples [7]–[9]. By imaging 2D tissue slices (or sections thereof), scanning span, and therefore acquisition time, is considerably reduced. However, does not address issue of the computationally intensive process of recovering the compressively sampled RCM images, which can take between 1 and >20 minutes for a single image recovery operation.

Recent advances have been made in successfully developing Deep-Learning-based approaches for accurate recovery of images from CS measurements [10], [11]. These works present alternative network architectures for the recovery of compressively sampled images into their corresponding 2D images. These architectures allow recovering CS images with





(a) Sample image from the natural (b) Sample image from the skin image training dataset.

slice image training dataset.

Fig. 2: Samples from the natural image and skin slice image training datasets, and their respective initial approximations  $x_0$ .

acceptable quality and execution times, and show that it is possible to exploit the advantages of both CS and CNNs in conjunction to perform close to real-time CS imaging. This paper presents the preliminary results of using CS to manage the current shortcomings of RCM devices (acquisition speeds limited by raster scanning), while using Deep Learning to manage the shortcomings of the CS framework (timeconsuming optimization-based recovery of images). Specifically, we employ the ISTA-Net [11] architecture for the specific case of recovering RCM images from CS samples at various parameter combinations. In addition, we propose an alternative architecture for the denoising of ISTA-Net recovered RCM images.

## II. RELATED WORK

# A. Optimization-Based Recovery

The pioneer work of Candès, Romberg and Tao [12] proposed the use of  $\ell_1$ -minimization for solving the underdetermined system given by the CS acquisition process. Common algorithms for recovering CS images using the  $\ell_1$ minimization approach include the  $\ell_1$ -magic [13] and TVAL3 [14]. Additionally, ISTA has been used to approximate the nonlinear deconvolution operator for image recovery from CS samples [15]. While these methods provide acceptable image recovery performance, they require long computation times, limiting the applications of CS to non-realtime imaging. In this work, we employ the use of an  $\ell_1$ -magic based, block CS algorithm for the acquisition and recovery of images for evaluating of the proposed architecture to an established, optimization-based method.

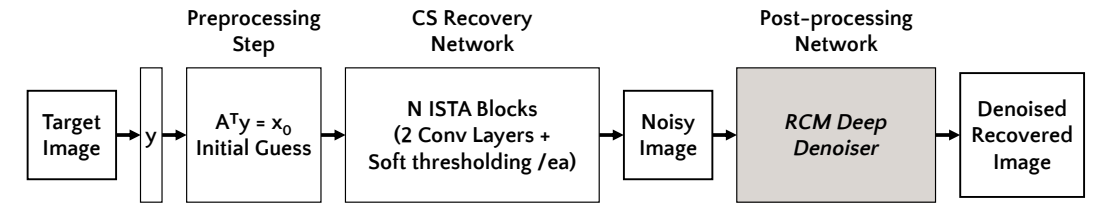
# B. Network-Based Recovery

There have been several neural network architectures proposed for the problem of CS-acquired image recovery. Most relevant to the current study, are Kulkarni's ReconNet [10], and Zhang's ISTA-Net [11]. Both of these approaches propose different network architectures for the successful recovery of CS measurements into their corresponding 2D images. Among these architectures, Zhang's approach consistently more accurate recovery of images (28.50 PSNR vs 26.46 PSNR), at the expense of image recovery rate (25.6 FPS vs 62.5 FPS). However, the fact that the state-of-the-art makes it possible to

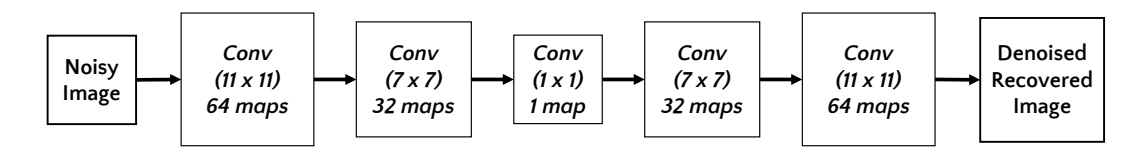
state the image recovery rates in FPS implies that it is possible to exploit the advantages of both CS and CNNs in conjunction to perform an approximation of real-time CS-based imaging. Additionally Chang . has proposed the Deep Residual Convolutional Neural Network-based Compressive Sensing Reconstruction (DRCNN-CSR) framework [16] in the context of microscopy, which makes use of the Residual Neural Network (RNN) architecture for recovery [17] of CS images. However, their acquisition procedure does not take into account recent integrations of the CS framework for sampling efficiency [7], [8]. The recovery of compressively sampled images is currently produced by three different architectures: ReconNet's approach is based on traditional CNNs, ISTA-Net is based on a truncated form of ISTA, and DRCNN-CSR is based on the concept of Residual Neural Networks [17], which are more resistant to the vanishing gradient problem during training, and allow for a distribution of weights that more efficiently make use of the available processing layers. For final post-processing, ReconNet employs an "off-shelf" denoiser. That is, a direct implementation of Dabov 's BM3D algorithm [18], which, on a blockwise manner, utilizes the sparse representation of similar blocks across the image as reference in order to preserve common features and discard noise. However, this iterative, adaptive algorithm must be executed for every recovered image, and can be detrimental in applications requiring near-real-time imaging rates. ISTA-Net, does not incorporate a post-processing step in its design, and DRCNN-CSR uses another Residual Neural Network for post-processing, with the only difference compared to its CS recovery step being a smaller amount of residual blocks. This architecture reuse can have the possible side effect of overfitting, and/or failing to generalize certain features better suited for other architectures.

# III. ISTA-NET+RCMDD

In order to further improve the performance of recovered images without the need of an iterative algorithm, such as the BM3D algorithm used in [10] which might impose additional computational strain on a mobile/embedded platform, we propose the separate training of a simple secondary denoiser network, called RCM Deep Denoiser (RCMDD). This network is proposed with a convolutional autoencoder architecture, which has established use in literature for medical image denoising [19]. The RCMDD is placed at the output of the final ISTA-Block, taking the ISTA-Net output as input. The RCMDD architecture consists of five layers: two convolutional layers decreasing in dimensionality (64, 32 feature maps), an arbitrary maximum compression layer (coding stage), and two convolutional layers increasing in dimensionality (32, 64 feature maps) to recover the target image from its encoded representation (decoding stage). A diagram for the entire CS RCM image recovery network and the proposed RCMDD network is presented in Figure 3.



(a) Proposed RCM image recovery framework, with the proposed RCMDD block highlighted in gray.



(b) Detailed view of the architecture for the proposed RCM Deep Denoiser network.

Fig. 3: Proposed framework for the accurate recovery of RCM CS images, showing the overall system architecture, and the architecture for the proposed RCMDD



Fig. 4: Sample  $33 \times 33$  SBHE pattern (Hadamard block size = 16) used to simulate CS acquisition of RCM images.

# A. CS Acquisition of RCM Images

With the objective of being consistent with the constraints of CS-based RCM imaging devices in literature, the sampling matrix A is generated to display Scrambled Hadamard Block Ensemble Patterns (SHBE), according to the findings of Wu [8]. These constraints state that the patterns must be binary, and that activated pixels are to be surrounded as much as possible by inactive pixels. In this approach, images are compressively sampled across the en-face plane. These considerations are focused on ensuring the optical sectioning capability of the CS-RCM device. A sample pattern used to simulate the CS acquisition of RCM images is presented in Figure 4.

In order to perform recovery of CS images, ISTA-Net requires an initial approximation of equal dimensionality to the target recovered image as its input, given by

$$x_0 = A^T y. (1)$$

While the initial approximation  $x_0$  describes abysmal image quality when compared to the original image x, it provides the image reconstruction network with enough information for recovery due to containing spatially contextual information of both the projections of the pixels in the original image x, and the patterns in A that dictate said projections.

Our training procedure for the ISTA-Net network is as follows: we selected to section images in 33 px  $\times$ 33 px blocks (in terms of CS, this makes our individual vectorized signals

of length  $N=1089 \mathrm{px}$  for each block). Consequently, the considered sampling rates of 10%, 25% and 50% yield a total of  $M=\{1089*0.1,\ 1089*0.25,\ 1089*0.5\}\approx\{109,272,545\}$  sampling operations, respectively, after performing CS acquisition using the SBHE patterns corresponding to each training data set. For consistency, the SBHE patterns for CS were randomly generated once, then saved for use in all applicable cases.

# B. ISTA-Net Recovery Parametrization

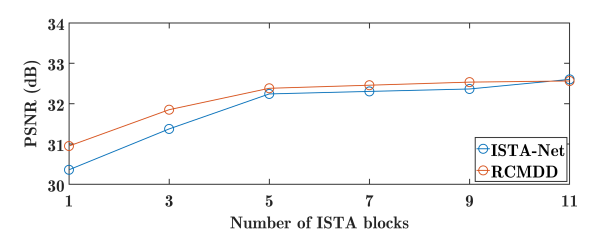
In order to adequately gauge the resolution of the recovered images (which is a very significant concern for clinical use of RCM skin images) using the ISTA-Net architecture and the USAF target image, we trained an individual network on natural images for each of six considered ISTA blocks in the network architecture: 1, 3, 5, 7, 9 and 11 blocks.

Our analysis brought to our attention the presence of obvious blocking artifacts on RCM images recovered from CS measurements using the ISTA-Net architecture. Figure 8 illustrates an example of this phenomenon.

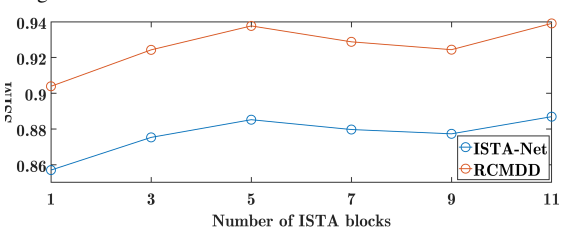
Additionally, while [11] suggests that a single ISTA-Net network is capable of recovering CS images sampled under a variety of undersampling rates, an initial test resulted in drastically reduced performance when undersampling rates were significally different from those used during network training. For this reason, the presented analysis will include a study of the influence of the undersampling rates on the recovery performance of CS RCM images. In total, our study compares the performance of the following six networks:

- 3 networks for Natural data: 10%, 25% and 50% sampling rates.
- 3 networks for Skin data: 10%, 25% and 50% sampling rates.

For training these networks, we used Adam optimization with a learning rate of 0.0001 over 80 epochs, and a batch size of 128.

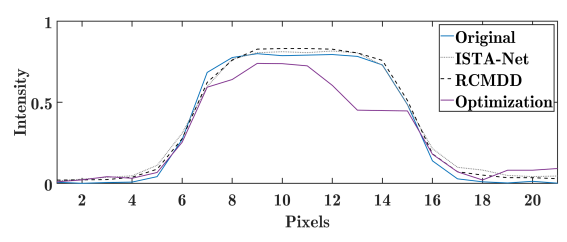


(a) Influence of the number of ISTA blocks on PSNR of recovered images.

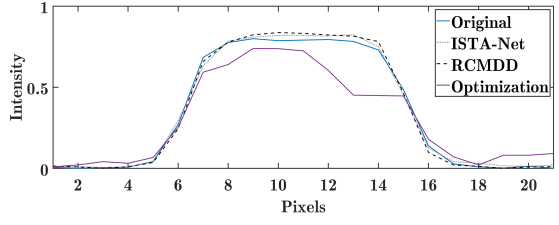


(b) Influence of the number of ISTA blocks on SSIM of recovered images.

Fig. 5: Image recovery performance for the proposed architecture.



(a) Intensity profile for USAF Target, 1 ISTA block.



(b) Intensity profile for USAF Target, 11 ISTA blocks.

Fig. 6: Intensity profiles of recovered images for resolution assessment.

In summary, the training process is performed in two stages: First, the ISTA-Net network is trained with initial approximations (given by Equation 1) from CS measurements as input data, and the original RCM images as target output data. Once trained, the ISTA-Net output is used as training inputs for the RCMDD, with the original RCM images as target output data.

A diagram for the proposed architecture is presented in Figure 3. Figure 3a shows the complete network architecture, incorporating ISTA-Net for initial recovery, and RCMDD for denoising. The convolutional autoencoder architecture used for RCMDD is presented in Figure 3b.

All accuracy results will be presented using the average Peak-Signal-to-Noise-Ratio (**PSNR**), as well as the Structural

Similarity Index (**SSIM**). We provide a qualitative analysis in the form of edge profiles for the considered RCM images. Figure 1 shows the spatial context of the regions of interest and profiles that will be presented. For a fuller comparison, we compare our results to those obtained using an optimization-based recovery approach (using  $\ell_1$ -magic) for RCM images, which are contextually illustrated in Figures 7 and 8.

#### IV. EXPERIMENTAL SETUP

# A. Data Sets

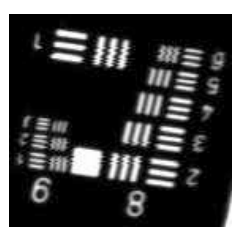
- 1) Training Data: In order to accurately evaluate the recovery performance of the ISTA-Net framework of these RCM images, we trained independent networks separately on both RCM skin data and the natural image dataset used in [10]. Single images from the skin image and natural image training datasets are presented in Figure 2. In order to adequately train the proposed network architecture on the widest range of morphological features present in highly heterogeneous skin tissue, we use 17 different skin stacks for training, which contain a total of 910 optically-sectioned single-channel slices, each containing 961 33px ×33px blocks. In summary, we generate a total of 874,510 blocks from this data for training. Due to computational constraints and to maintain reasonable training times, a subset of 500,000 blocks were randomly selected for training our RCM ISTA-Net network.
- 2) Testing Data: In order to objectively evaluate the performance of CS images recovered by the proposed architecture, we perform preliminary testing on a copy of the U.S. Air Force Test Chart (USAF-1951) target, used commonly in image equipment resolution assessment. The test chart was captured using a a clinical confocal microscope [Vivascope 1500, Caliber Imaging and Diagnostics (formerly, Lucid Inc., Rochester)], with 830nm illumination and a 30x, 0.9 numerical aperture, gel immersion objective lens. The optical sectioning thickness is  $2\,\mu\mathrm{m}$  for each slice, and lateral resolution 0.5 m. The field of view is 0.5 mm. The single-channel acquired images have a size of is  $1000\times1000$  pixels.

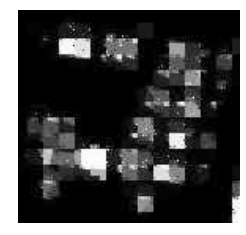
Further, for the purposes of evaluating the reconstruction performance of the algorithm on real skin data, we used a skin stack captured  $in\ vivo$  at a size of  $1000\times1000$  pixels using the same RCM device. The captured USAF-1951 target and skin stack slice images used for this analysis are shown on Figure 1.

## V. RESULTS

#### A. ISTA-block count influence on recovery performance

In this section, we will present the summarized results of our analysis on both RCM image types. The influence of the number of ISTA-blocks in the recovery network for recovery of the USAF image is presented in Figure 5. Further, sample intensity profiles for the extreme cases of 1 and 11 ISTA-blocks are presented in Figure 6. Numerical results of the influence of ISTA-blocks on recovery performance, in the form of PSNR and SSIM values, are summarized in Table I. It is important to highlight that the presented values for skin images on Table I do not correspond to a single slice, but are average

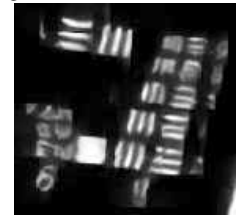




used for testing

(a) USAF Target reference image (b) Recovered USAF Target image using  $\ell_1$ -minimization





using ISTA-Net

(c) Recovered USAF Target image (d) Recovered USAF Target image using RCMDD

Fig. 7: Reference and recovered USAF Target images using the considered methods using a 10% sampling rate.

# ISTA-Blocks	Data Type	PSNR (dB)		SSIM		
		ISTA-Net	RCMDD	ISTA-Net	RCMDD	
1	Natural	30.3614	30.9498	0.8570	0.9039	
3	Natural	31.3731	31.8496	0.8753	0.9243	
5	Natural	32.2402	32.3799	0.8852	0.9377	
7	Natural	32.3027	32.4563	0.8797	0.9288	
9	Natural	32.3629	32.5328	0.8773	0.9244	
11	Natural	32.6008	32.5612	0.8869	0.9391	
1	Skin	23.6025	23.7053	0.4994	0.5013	
3	Skin	23.6459	23.7461	0.5013	0.5029	
5	Skin	23.7163	23.8091	0.5025	0.5039	
7	Skin	23.6871	23.7757	0.4987	0.5003	
9	Skin	23.7642	23.8528	0.5052	0.5062	
11	Skin	23.7282	23.8111	0.5017	0.5025	

TABLE I: Numerical image recovery results for different ISTA-block sizes for both natural and skin RCM CS images.

values for all images in a test 45-slice RCM skin stack. The intensity profiles presented in Figure 6 indicate that both of the considered approaches have a practically equal capacity of edge preservation in recovered images, and surpass that of the previously established optimization-based approach. This is highlighted due to the importance of morphological features in skin RCM images for diagnostic purposes. Further, the results presented in Figure 5 indicate that, when taking into account the benefits of a fast, lightweight recovery network for recovery of RCM images, there is a case of diminishing returns on the quality of recovery images when using a recovery network with more than 5 ISTA-blocks. This is further confirmed for the case of skin images by inspecting the results in Table I. For this reason, our experiments for the rest of the document will set the ISTA block number in the recovery networks to 5. The average slice recovery times from its CS samples for ISTA-Net, ISTA-Net+RCMDD, and the  $\ell_1$ minimization based recovery method are 0.0851s (11.75 FPS), 0.1005s (9.95 FPS), and 917.7353 (<1 FPS), respectively.

# B. Sampling rate influence on recovery performance

Table II presents the numerical results from our study on the influence of sampling rate on the performance of recovered images using ISTA-Net, RCMDD and the method utilized in [6]. In addition to this, visual results for qualitative analysis comparing the target image and its recoveries from CS measurements at 10% sampling rate using the considered methods is presented in Figure 7. Naturally, higher sampling rates produce higher quality results. In addition to this, the proposed RCMDD architecture shows an increase in the performance of recovered images for both of the considered data types. Finally, we present sample recovered images from CS measurements in Figure 8 for qualitative evaluation at a sampling rate of 10%.

## VI. CONCLUSIONS AND FUTURE WORK

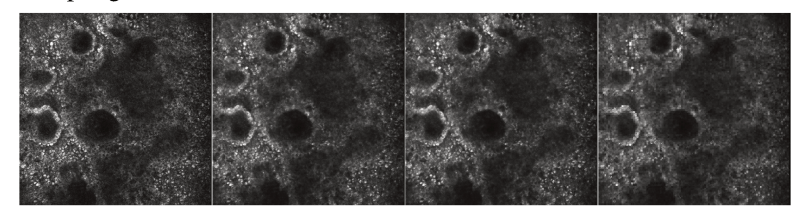
Deep Learning approaches are continuously proving their capacity for a variety of image processing and transformation tasks. We have proposed an architecture that further improves the capacity of the ISTA-Net architecture for recovering CS images acquired using an RCM device. For the purposes of increasing the quality of the recovered images, we have performed a comparative study of the parametrization of the proposed architecture with state-of-the-art methods. Our results conclude that, for the purposes of balancing image quality, network complexity and acquisition times, a total of 5 ISTA blocks is an appropriate architecture design parameter for the recovery network. On the subject of sampling rates, as intuition would suggest, higher sampling rates produce higher quality results. However, in addition to concerns about optical bleaching of tissues due to light exposure common in skin RCM imaging, there exists a trade-off between the selected CS sampling rate and imaging rates. The presented preliminary quantitative and qualitative results suggest that, upon fine adjustment of the involved acquisition system and proposed recovery architecture parameters, it is possible to recover images from CS measurements with higher performance levels for a given sampling rate. By bypassing the requirement for solving a computationally costly optimization problem for recovering an image from its CS measurements, a CS-based, efficient, and real-time RCM imaging system becomes possible. However, this comes at the cost of the introduction of data-specific biases into the recovery network behavior, which is highlights the importance of sourcing and adequately constraining the application-specific training data to the relevant applications. Future work on this matter includes performing a more thorough analysis over a wider range of architecture design parameters, consulting experienced clinical personnel in order to gain firsthand insights about the clinical usability of the recovered images, and evaluate potential modifications to the RCMDD network architecture.

# REFERENCES

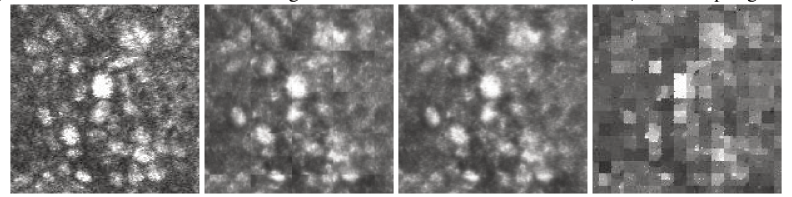
- [1] M. Rajadhyaksha, M. Grossman, D. Esterowitz, R. H. Webb, and R. R. Anderson, "In vivo confocal scanning laser microscopy of human skin: melanin provides strong contrast," Journal of Investigative Dermatology, vol. 104, no. 6, pp. 946-952, 1995.
- [2] T. Wilson, "Confocal microscopy," Academic Press: London, etc, vol. 426, pp. 1-64, 1990.
- [3] G. Pellacani, P. Guitera, C. Longo, M. Avramidis, S. Seidenari, and S. Menzies, "The impact of in vivo reflectance confocal microscopy for the diagnostic accuracy of melanoma and equivocal melanocytic lesions," Journal of Investigative Dermatology, vol. 127, no. 12, pp. 2759-2765, 2007.

Sampling Rate (%)	Data Type	ISTA-Net PSNR (dB)	RCMDD PSNR (dB)	$\ell_{-}1$ min. PSNR (dB)	ISTA-Net SSIM	RCMDD SSIM	$\ell$ _1 min. SSIM
10	Natural	29.8616	32.2402	21.1288	0.9359	0.9377	0.8809
25	Natural	30.8037	34.5328	25.9876	0.9491	0.9696	0.9443
50	Natural	31.6479	38.8765	33.0035	0.9566	0.9853	0.9804
10	Skin	23.7300	23.8198	22.5587	0.5016	0.5034	0.4740
25	Skin	25.7581	25.8596	24.7859	0.6663	0.6793	0.6451
50	Skin	28.1792	29.2442	27.9012	0.8099	0.8544	0.8370

TABLE II: Numerical image recovery results for images acquired and recovered using networks trained for the recovery of each specific data type and sampling rate.



(a) Full 1mm×1mm skin slice images recovered from CS measurements (10% sampling rate).



(b) Zoomed sections of skin slice images recovered from CS measurements (10% sampling rate).

Fig. 8: From left to right: Reference image, ISTA-Net output, RCMDD output, optimization-based approach output.

- [4] J. Zitelli, F. Mohs, P. Larson, and S. Snow, "Mohs micrographic surgery for melanoma." *Dermatologic clinics*, vol. 7, no. 4, pp. 833–843, 1989.
- [5] H. Sierra, B. A. Larson, C.-S. J. Chen, and M. Rajadhyaksha, "Confocal microscopy to guide erbium: yttrium aluminum garnet laser ablation of basal cell carcinoma: an ex vivo feasibility study," *Journal of biomedical* optics, vol. 18, no. 9, pp. 095 001–095 001, 2013.
- [6] F. X. Arias, H. Sierra, M. Rajadhyaksha, and E. Arzuaga, "Compressive sensing in reflectance confocal microscopy of skin images: a preliminary comparative study," in *Three-Dimensional and Multidimensional Microscopy: Image Acquisition and Processing XXIII*, vol. 9713. International Society for Optics and Photonics, 2016, p. 97130Z.
- [7] P. Ye, J. Paredes, Y. Wu, C. Chen, G. Arce, and D. Prather, "Compressive confocal microscopy: 3d reconstruction algorithms," in SPIE MOEMS-MEMS: Micro-and Nanofabrication. International Society for Optics and Photonics, 2009, pp. 72 100G–72 100G.
- [8] Y. Wu, P. Ye, I. O. Mirza, G. R. Arce, and D. W. Prather, "Experimental demonstration of an optical-sectioning compressive sensing microscope (csm)," *Optics express*, vol. 18, no. 24, pp. 24565–24578, 2010.
- [9] N. Pavillon and N. Smith, "Compressed sensing laser scanning microscopy," *Optics express*, vol. 24, no. 26, pp. 30 038–30 052, 2016.
- [10] K. Kulkarni, S. Lohit, P. Turaga, R. Kerviche, and A. Ashok, "Reconnet: Non-iterative reconstruction of images from compressively sensed measurements," in *Proceedings of the IEEE Conference on Computer Vision and Pattern Recognition*, 2016, pp. 449–458.
- [11] J. Zhang and B. Ghanem, "Ista-net: Iterative shrinkage-thresholding algorithm inspired deep network for image compressive sensing," 2017.
- [12] E. J. Candès, J. Romberg, and T. Tao, "Robust uncertainty principles: Exact signal reconstruction from highly incomplete frequency information," *Information Theory, IEEE Transactions on*, vol. 52, no. 2, pp. 489–509, 2006.
- [13] E. Candes and J. Romberg, "11-magic: Recovery of sparse signals via convex programming," *URL: www. acm. caltech. edu/11magic/downloads/11magic. pdf*, vol. 4, p. 14, 2005.
- [14] C. Li, W. Yin, and Y. Zhang, "User's guide for tval3: Tv minimization by augmented lagrangian and alternating direction algorithms," *CAAM* report, vol. 20, no. 46-47, p. 4, 2009.
- [15] Y. Zhang, S. Wang, G. Ji, and Z. Dong, "Exponential wavelet iterative shrinkage thresholding algorithm with random shift for compressed sensing magnetic resonance imaging," *IEEJ Transactions on Electrical* and Electronic Engineering, vol. 10, no. 1, pp. 116–117, 2015.

- [16] K.-Y. Chang, Y.-L. Liu, D.-W. Liu, M.-H. Chou, J.-W. Wu, and L.-C. Fu, "A fast clsm undersampling image reconstruction framework with precise stage positioning for random measurements," in *Control Conference (ASCC)*, 2017 11th Asian. IEEE, 2017, pp. 1122–1127.
- [17] K. He, X. Zhang, S. Ren, and J. Sun, "Deep residual learning for image recognition," in *Proceedings of the IEEE conference on computer vision* and pattern recognition, 2016, pp. 770–778.
- [18] K. Dabov, A. Foi, V. Katkovnik, and K. Egiazarian, "Image denoising by sparse 3-d transform-domain collaborative filtering," *IEEE Transactions* on image processing, vol. 16, no. 8, pp. 2080–2095, 2007.
- [19] L. Gondara, "Medical image denoising using convolutional denoising autoencoders," in 2016 IEEE 16th International Conference on Data Mining Workshops (ICDMW). IEEE, 2016, pp. 241–246.